

## 13

# Perovskites Enabled Highly Sensitive and Fast Photodetectors

Nicholas Lauerstorff<sup>1</sup> and Jinsong Huang<sup>2</sup>

<sup>1</sup>University of North Carolina at Chapel Hill, Department of Applied Physical Sciences, 121 South Rd., 1129 Murray Hall, Chapel Hill, NC 27599, USA

<sup>2</sup>University of North Carolina at Chapel Hill, Department of Applied Physical Sciences, 121 South Rd., 1115 Murray Hall, Chapel Hill, NC 27599, USA

## 13.1 Introduction

Recently, perovskites have gained much attention due to the unprecedented improvement of their record power conversion efficiency (PCE), with perovskite solar cells reaching up to 25.5% [1]. The optoelectronic properties of perovskite, such as high absorption coefficient [2], long carrier diffusion lengths [3], superior charge carrier mobility [4], and generation of free charge carriers by photoexcitation [5], translate well to many other device applications, namely, photodetectors.

A photodetector is a device that senses the presence of light by converting optical signal of a specific wavelength range to electrical signals. Next-generation perovskite photodetectors have gained increasing interest due to their widespread applications in spectroscopy, image sensing, biological/chemical/radiation sensing, environmental monitoring, and fiber-optic communication. The ideal properties of these photodetectors are fast response speed, high signal, large linear response range, low noise, and controllable, wavelength-dependent response. Each application has different performance requirements, necessitating photodetector optimization. Photodetector applications generally emphasize either very high sensitivity (spectroscopy, imaging, and remote sensing) or very high modulation frequencies (data communication, time-of-flight remote sensing, and temporal spectroscopy measurements) [6].

## 13.2 Why Perovskites for Photodetectors

Silicon is the most utilized commercial visible-light photodetector. However, it has high sensitivity outside of the visible spectrum.  $\text{MAPbI}_3$  (MA = methylammonium) and crystalline silicon have absorption coefficients of  $5 \times 10^3$ – $5 \times 10^4 \text{ cm}^{-1}$  [7] and  $6 \times 10^3$ – $8 \times 10^2 \text{ cm}^{-1}$ , respectively, in the wavelength range of 500–800 nm [8].

In addition to having much higher absorption coefficients, perovskites are insensitive to IR light, enabling light detection without the need for external optical filters [9]. Perovskites absorb a much greater number of photogenerated charge carriers per unit of thickness, improving the external quantum efficiency (EQE) and enabling near complete absorption of incident light with only a few-hundred-nanometer-thick film [10, 11].

Responsivity ( $R$ ) quantifies how efficiently a photodetector responds to optical signal at various wavelengths and can be thought of as the electrical output per optical input. It is defined as

$$R(\lambda) = \frac{I_{\text{ph}}}{P_{\text{in}}} = \frac{\text{EQE} * q}{h * v} (\text{A/W}) \quad (13.1)$$

where  $I_{\text{ph}}$  is the photocurrent,  $P_{\text{in}}$  is the incident light power,  $q$  is the elementary charge,  $v$  is the frequency of light, and  $h$  is Planck's constant. It is best to operate a photodetector such that it is measuring light at or around the wavelength of highest responsivity, resulting in the largest signal-to-noise ratio (SNR) and sensitivity. Maximum responsivity generally corresponds to photon energies just above that of the photoactive material's bandgap.

Unlike silicon, perovskites benefit from a sharp absorption edge due to their direct bandgap, enabling well-defined regions of either high or low responsivity [12, 13]. Perovskite photodetectors also have an easily tunable response range. Changing the  $\text{ABX}_3$  composition in any way will have some effect on the bandgap and, therefore, shift the response range from ultraviolet to near IR (nIR), but altering the halide component has the largest and most easily controllable influence [11, 14, 15].

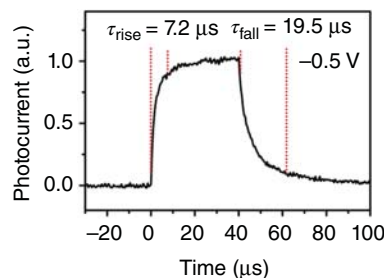
Charge carriers must quickly reach and recombine at the electrodes as determined by the mobility and transit distance, which are limited by defect/trap density. Due to their efficient charge balancing of point defects, perovskites are very difficult to dope, resulting in near-intrinsic performance [16]. In addition, they have a high defect tolerance. The low concentration of intrinsic defects consists mostly of shallow traps, hindering efficient charge transport as opposed to promoting recombination [17, 18]. As a result, perovskites have very high charge carrier mobilities, typically in the tens of  $\text{cm}^2/(\text{V s})$ , enabling high EQE and low response time [19].

The response time ( $\tau_r$ ) describes the time it takes for both photogenerated minority ( $\tau^p$ ) and majority carriers ( $\tau^n$ ) to reach their respective electrodes and recombine. This is parameterized as the greater of either rise time ( $\tau_{\text{rise}}$ ) or fall time ( $\tau_{\text{fall}}$ ). Rise time is the time required for the signal to increase from 10% to 90% of its maximum value, whereas fall time is the time required for the signal to decrease from 90% to 10% of its maximum value (Figure 13.1). Response time is typically limited by three factors: the RC time constant ( $\tau_{\text{RC}}$ ), the drift component  $\tau_{\text{drift}}$ , and the diffusion component ( $\tau_{\text{diff}}$ ):

$$\tau_r = \sqrt{(2.2\tau_{\text{RC}})^2 + \tau_{\text{drift}}^2 + \tau_{\text{diff}}^2} \quad (13.2)$$

The rate of charge trapping and de-trapping, accounted for in  $\tau_{\text{RC}}$ , is the major limiting factor [20–22]. Upon illumination, photogenerated charge carriers accumulate

**Figure 13.1** Rise and fall times given for a single normalized cycle of an  $\alpha$ -FAPbI<sub>3</sub> (FA = formamidinium) photodetector's photocurrent at a frequency of 500 Hz. Source: Zhang et al. [15]. Licensed under CC BY 4.0.



at the perovskite interfaces, which can be trapped in lattice defects and change the capacitance [23].

Mobile ions and charge defects also aggregate at grain boundaries, screening the built-in potential [24–27]. These moving charges contribute to the capacitance spectrum [28]. The opposing electrostatic potential alters the interfacial charge carrier concentration and recombination rates, in turn decreasing induced photocurrent and increasing  $\tau_{RC}$  [29–31]. Additive engineering and surface treatments have been a prime focus to passivate both surface and bulk defects and reduce ion migration [5, 32, 33].

Trapping, de-trapping, and recombination of charge carriers also result in electronic noise, with deep-trap-mediated recombination dominating under illumination [34]. This trap-induced current fluctuation manifests as the 1/f, or flicker, noise [35, 36]. There are two other major sources of noise: Johnson–Nyquist (thermal) and dark noise. We define the average noise spectral density as

$$\begin{aligned} \langle i_n^2(\omega) \rangle &= \left[ 2q\langle i_d \rangle + \frac{4k_B T}{R_{\text{shunt}}} + i_{\frac{1}{f}}^2(\omega) \right] \Delta f \\ &= [\text{shot noise} + \text{Johnson noise} + \text{Flicker noise}] \Delta f \end{aligned} \quad (13.3)$$

where  $\langle i_d \rangle$  is the average dark current,  $T$  is the temperature,  $k_B$  is the Boltzmann constant,  $R_{\text{shunt}}$  is the shunt resistance,  $i_{\frac{1}{f}}^2(\omega)$  is the flicker noise spectral power density, and  $\Delta f$  is the frequency bandwidth. Due to the relatively low deep-trap density, perovskites have a small flicker noise [37–39].

This noise spectrum is more practically quantified as the noise equivalent power (NEP), which is where the SNR is equal to 1 with respect to incident light intensity:

$$\text{NEP} = \frac{i_n}{R(\lambda)} \text{ (W)} \quad (13.4)$$

A small NEP benefits two important parameters: linear dynamic range (LDR) and specific detectivity ( $D^*$ ). LDR can similarly be thought of as the range in which responsivity of the photodetector is constant with respect to the incident light intensity, setting its lower limit:

$$\text{LDR} = 20 \log \left( \frac{J_{\text{upper}} - J_d}{J_{\text{lower}} - J_d} \right) \text{ (dB)} \quad (13.5)$$

$J_{\text{upper}}$  is the current at which responsivity deviates from linearity,  $J_{\text{lower}}$  is the lower resolution limit, and  $J_d$  is the dark current.

Specific detectivity ( $D^*$ ) tends to be used as a universal means of comparing performance between various photodetectors:

$$D^* = \frac{\sqrt{A\Delta f}}{\text{NEP}} = \frac{R(\lambda)\sqrt{A\Delta f}}{i_n} \text{ (Jones)} \quad (13.6)$$

where  $A$  is the active area.  $D^*$  can be interpreted as SNR generated by a photodetector with incident area of  $1 \text{ cm}^2$  at  $1 \text{ W}$  of incident power when the electrical bandwidth ( $\Delta f$ ) is  $1 \text{ Hz}$ , normalizing performance with respect to the active area and bandwidth of the device that prevents severe overestimation for small area devices. NEP varies with frequency; therefore, it is important to report the frequency at which the specific detectivity is calculated at as well.

### 13.3 Types of Perovskite Photodetectors

There are three types of photodetectors: photoconductors, phototransistors, and photodiodes. Each of these devices has their own benefits for different applications and their own shortcomings.

#### 13.3.1 Photodiodes

Photodiodes are by far the most researched photodetector in the field of perovskite due to the similar device structure to solar cells and the ability to operate efficiently at low or no applied voltage bias. These are commonly used in fiber-optic communication [40], medical imaging [41], and consumer electronics [42]. A perovskite photodiode is a vertical p-i-n junction typically with an inverted device structure (Figure 13.2).

Photodiodes emphasize low noise and fast charge collection under reverse bias. They typically have a much more linear response to light than photoconductors. In addition, photodiodes generally cannot have a photoconductive gain greater than unity. These properties are due to interfacial charge transport layers that prevent charge injection into the perovskite. Furthermore, interfacial layers passivate defect-rich surfaces, reducing flicker noise [46]. Dark current is also minimized by operating many perovskite photodiodes at  $0 \text{ V}$  bias.

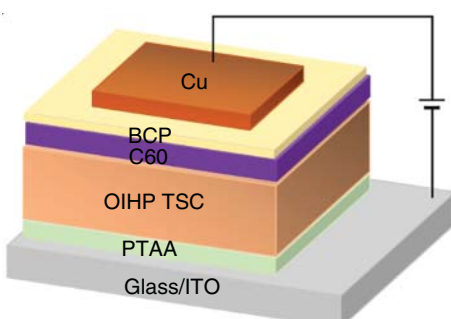


**Figure 13.2** Typical photodetector device structure of substrate/cathode/HTL/photoactive material/ETL/anode. Bathocuproine (BCP) acts as both hole blocking and electron transport material, while PTAA acts as both electron blocking and hole transport material.  $C_{60}$  is similarly used as an interfacial buffer layer to reduce charge accumulation [43, 44]. Source: Bao et al. [45].

### 13.3.1.1 Broadband Photodiodes

Dou et al. fabricated three devices with either a bathocuproine (BCP) hole-blocking layer (HBL), a poly[(9,9-bis(30-(*N,N*-dimethylamino)propyl)-2,7-fluorene)-alt2,7-(9,9-dioctylfluorene)] (PFN) HBL, or without a HBL [47]. Operating at a small reverse bias of  $-100\text{ mV}$ , the control device without a HBL suffered from a large dark current density of  $10^{-7}\text{ A/cm}^2$  and low specific detectivity of  $3 \times 10^{11}\text{ Jones}$  at  $\lambda = 550\text{ nm}$ . Using HBLs of either BCP or PFN, specific detectivity increased to  $2 \times 10^{12}\text{ Jones}$  and  $8 \times 10^{13}\text{ Jones}$ , respectively, due to the enhanced electron injection, significantly decreasing leakage current. The device also showed a large LDR of over 100 dB, comparable with the 120 dB LDR of Si photodetectors, and fast rise and fall times of 180 and 160 ns, respectively.

Gong found that a fullerene derivative PCBM ([6,6]-phenyl-C<sub>61</sub>-butyric acid methyl ester) more efficiently facilitates charge carrier transport in addition to passivating the TiO<sub>2</sub>, leading to a significantly reduced leakage current under reverse bias [48]. The device achieved specific detectivity greater than  $4 \times 10^{12}\text{ Jones}$  and EQE greater than 80% at  $375\text{ nm} \leq \lambda \leq 800\text{ nm}$ . Relatively high dark current occurred due to the hole injection at the perovskite/cathode interface for typical fullerene derivative interlayers. Teng et al. added polymethyl methacrylate (PMMA) to PCBM to reduce the work function and improve hole-blocking properties [49]. This photodetector achieved consistently high specific detectivities of  $\sim 10^{13}\text{ Jones}$ , which is comparable with Si photodetectors in the visible range (Figure 13.3). In addition, it reached an LDR of 112 dB, and fall time decreased from  $2.7\text{ }\mu\text{s}$  (0 wt% PMMA) to  $2.2\text{ }\mu\text{s}$  (20 wt% PMMA) due to the introduction of slightly more recombination centers.

Fang et al. confirmed that a C<sub>60</sub> buffer layer significantly reduces dark current [46]. Using PEDOT:PSS (poly(3,4-ethylenedioxythiophene) poly(styrenesulfonate)) as the hole transport layer (HTL) and PCBM/C<sub>60</sub> (20 nm/20 nm) as the electron transport layer (ETL), reverse bias dark current was reduced to  $1.6 \times 10^{-7}\text{ A/cm}^2$ . This result is one order of magnitude smaller than those reported by Dou et al. who did not use C<sub>60</sub> [47]. As demonstrated by Wang et al., this is because the C<sub>60</sub> layer reduces dark current leakage by forming a Schottky junction with the anode, and effectively

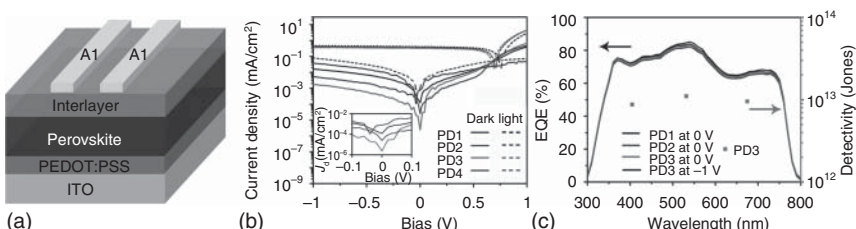


**Figure 13.3** (a) Schematic of ITO/PEDOT:PSS/perovskite/PCBM:PMMA/Al photodetector. (b)  $J$ - $V$  (current density-voltage) characteristics of PCBM:PMMA hybrid photodetectors under dark and 532 nm ( $1\text{ mW/cm}^2$ ) light illumination. Inset:  $J$ - $V$  characteristics of the photodetectors under  $-100\text{ mV}$  through  $+100\text{ mV}$  bias voltage in a semi-log scale. (c) EQE spectra (solid line) of the hybrid photodetectors at different reverse bias and the detectivity (square points) of PD3 at  $\lambda = 405, 532$ , and  $675\text{ nm}$ . Source: Feng Teng et al. [49].

passivating traps in the perovskite layer [50]. Replacing PEDOT:PSS with OTPD (*N*4,*N*4'-bis(4-(6-((3-ethyloxetan-3-yl)methoxy)hexyl)phenyl)-*N*4,*N*4'-diphenylbi-phenyl-4,4'diamine) (a triphenylamine derivative) and increasing the thickness of the  $C_{60}$  from 20 to 80 nm suppressed the dark current to  $9.1 \times 10^{-9} \text{ A/cm}^2$  at  $-2 \text{ V}$ , more than 50 times smaller than the previously reported best perovskite photodetector [47]. This record photodetector achieved a responsivity of  $0.21 \text{ A/W}$ , comparable with those without the additional buffer layers, indicating that charge extraction is not impeded. This photodetector also achieved a record low NEP of  $4.3 \times 10^{-14} \text{ W/Hz}^{1/2}$  at  $\lambda = 560 \text{ nm}$ , resulting in an LDR of  $94 \text{ dB}$  and a lowest detectable intensity of  $0.64 \text{ pW/cm}^2$ . The detector maintained a specific detectivity greater than  $1 \times 10^{12} \text{ Jones}$  from  $330 \text{ nm} \leq \lambda \leq 790 \text{ nm}$ , reaching a maximum value of  $7.4 \times 10^{12} \text{ Jones}$  at  $\lambda = 680 \text{ nm}$  [46].

Lin et al. fabricated four devices with varying thicknesses of PCBM and  $C_{60}$  buffer layers (Figure 13.4a,b) [51], which demonstrated the lowest dark current of  $5 \times 10^{-10} \text{ A/cm}^2$  (Figure 13.4c). This results in a large LDR of  $\sim 170 \text{ dB}$  at  $-0.5 \text{ V}$ , small NEP of  $\sim 200 \text{ fW/Hz}^{1/2}$ , specific detectivity of  $>10^{12} \text{ Jones}$  in the UV–Vis spectrum, and completely blind response in the nIR, demonstrating its potential for imaging applications (Figure 13.4d).

Bao et al. utilized space-confined inverse-temperature crystallization in order to grow thin single crystals with a few to tens of microns thickness (Figure 13.2) [45, 52]. The detectors achieved a low noise of  $1\text{--}2 \text{ fA/Hz}$  at  $8 \text{ Hz}$ , yielding a

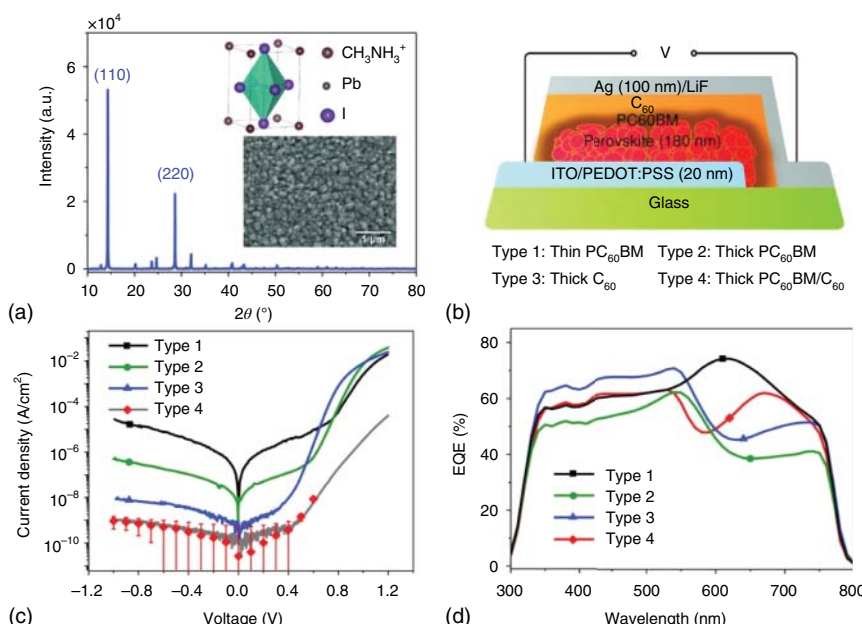


**Figure 13.4** (a) X-ray diffraction (XRD) spectrum of  $\text{MAPbI}_3$  on ITO/PEDOT:PSS. (b) Schematic of four different device structures tested. (c) Dark current  $J$ – $V$  characteristics at a scanning rate of  $1 \text{ mV/s}$ . (d) EQE spectra of all four devices. Source: Lin et al. [51].

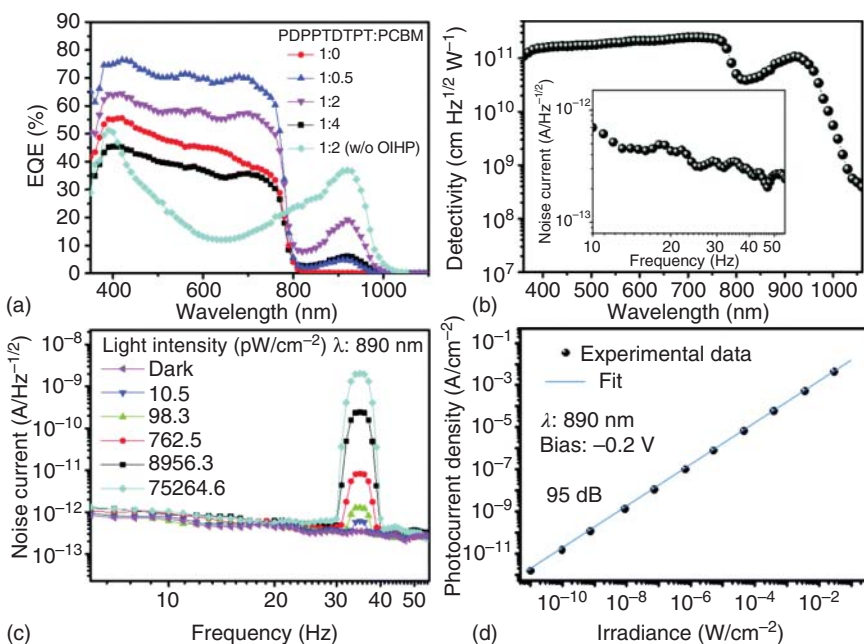


**Figure 13.5** (a) EQE values of hybrid photodetectors with different PDPPTDTPT:PCBM ratios at a bias of  $-0.2$  V. (b) Specific detectivity of hybrid photodetectors at different wavelengths at a  $-0.1$  V bias. (c) Noise currents of hybrid photodetectors in the dark and illuminated by  $\lambda = 890$  nm at different intensities. (d) LDR of the hybrid photodetector with  $\lambda = 890$  nm at various intensities. Source: Shen et al. [53].

high specific detectivity and an LDR of  $1.5 \times 10^{13}$  Jones and 256 dB, respectively, for  $\text{MAPbBr}_3$ . These devices performed similarly. The device's response time of hundreds of nanoseconds was limited by the thickness.

Pure Pb-based perovskite can only absorb  $\lambda < 800$  nm due to its wide bandgap, but hybrid detectors can extend the response range. Shen et al. developed a hybrid  $\text{MAPbI}_3$  photodetector utilizing a narrow bandgap PDPPTDTPT:PCBM (poly{2,5-bis(2-hexyldecyl)-2,5-dihydropyrrolo[3,4-c]pyrrole-1,4-dione-3,6-di(5-thiophen-2-yl)yl-*alt*-*N*-(2-ethylhexyl)-dithieno-[3,2-*b*:2,3-*d*]pyrrole-2,6-diyl}:phenyl- $C_{61}$ -butyric acid methyl ester) polymer, serving as both light-absorbing layer, charge transport layer, and barrier to charge injection from the cathode [53]. The dark current was reduced to as low as  $8.7 \times 10^{-8} \text{ A/cm}^2$  at a  $-0.3$  V bias, achieving NEP of  $5 \text{ pW/cm}^2$  and specific detectivity of  $1 \times 10^{11}$  Jones at 900 nm. The response range was extended to  $\sim 1000$  nm with an LDR of 95 dB (Figure 13.5).

Su et al. reported a self-powered photodetector (SPPD) (Figure 13.6) that utilizes both the photoelectric and triboelectric effects [54]. When an external force brings the top copper electrode into repeated contact periodically with the perovskite layer, triboelectric charges of opposite signs on the contacts induce an open-circuit voltage between the two electrodes. The triboelectric mechanism is highly responsive to incident light intensity, enabling a new mechanism for perovskite photodetection. This SPPD achieves broadband detection in the  $300 \leq \lambda \leq 1000$  nm range, an average responsivity of  $7.5 \text{ V/W}$ , and response time of 80 ms.

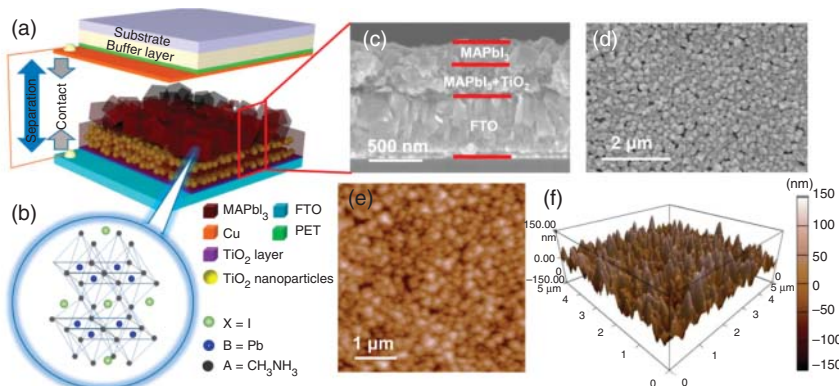


**Figure 13.6** (a) Device structure of an SPPD. (b) 3D crystal representation of MAPbI<sub>3</sub>. (c) Cross-sectional and (d) top-down views of the MAPbI<sub>3</sub>-based film performed via SEM. (e) Morphology of the MAPbI<sub>3</sub> capping layer measured via AFM. Source: Reprinted with permission from Su et al. [54]. Copyright 2015 American Chemical Society.

With an ITO/PEDOT:PSS/PbS QD/MAPbI<sub>3</sub>/PCBM/Al device structure, Gao et al. achieved broadband response from 375 to 1100 nm. PbS quantum dots (QDs) serve as a broadband light sensitizer in the Vis/nIR spectra, whereas MAPbI<sub>3</sub> serves as both a trap state passivator of the QD surfaces and a visible-light sensitizer [55]. Zhang et al. demonstrated that the addition of a separate photoactive layer of PbS QDs is found to dramatically enhance absorption in the UV–Vis spectrum while simultaneously providing a notable nIR response (Figure 13.7) [56]. Liu et al. obtained responsivities and specific detectivities of 0.302 A/W and  $1.2 \times 10^{13}$  Jones and 0.132 A/W and  $5.1 \times 10^{12}$  Jones at  $\lambda = 500$  nm and 900 nm, respectively, obtaining record performance for PbS-based photodetectors reported up to this point [57].

When deposited as separate layers, there was incomplete passivation of the QD surfaces, but, when deposited as a mixed solution, the quantum dot in

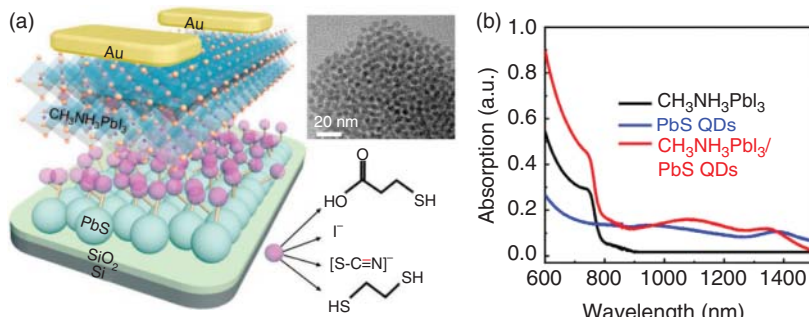


**Figure 13.7** (a) Device structure of the broadband PbS/CH<sub>3</sub>NH<sub>3</sub>PbI<sub>3</sub> composite photodetector and schematic diagram of the ligands used for exchange. Inset: TEM data of the oleic acid (OA)-capped PbS QDs. (b) Absorption spectra of CH<sub>3</sub>NH<sub>3</sub>PbI<sub>3</sub>, PbS CQDs, and PbS/CH<sub>3</sub>NH<sub>3</sub>PbI<sub>3</sub> composite films, demonstrating the broadening of the photodetector's response range. Source: Reprinted with permission from Zhang et al. [56]. Copyright 2019 American Chemical Society.

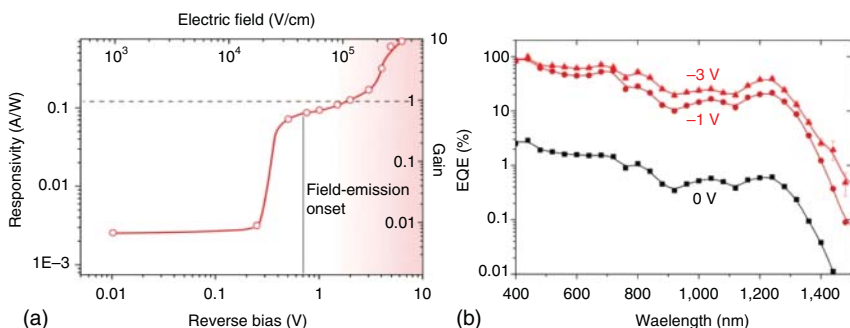


**Figure 13.8** (a) At  $-1\text{ V}$  bias, the responsivities maintained a linear relationship at intensities up to  $0.1\text{ mW/cm}^2$  using  $\lambda = 975\text{ nm}$  light, yielding an LDR of  $60\text{ dB}$ . (b) EQE values of  $\text{MAPbI}_{2.5}\text{Br}_{0.5}\text{:PbS}$  colloidal QD photodetector under different biases. A 60-fold increase is clear at the exciton peak. Source: Pelayo et al. [60]. Licensed under CC BY 4.0.

perovskite (QDiP) solution can form a well-passivated and highly tunable poly-heterocrystalline film as demonstrated by Ning et al. [58]. Clifford et al. developed an  $\text{MAPbI}_{2.5}\text{Br}_{0.5}\text{:PbS}$  colloidal QD device where excitons are photo-generated and confined within the PbS quantum dots [59, 60]. Once an electric field is large enough, the excitons separate, and the charge carriers are ejected. This is demonstrated with a sudden 45-fold increase in responsivity at  $-0.5\text{ V}$  bias. Specific detectivity reached  $5 \times 10^{12}\text{ Jones}$  in the visible spectrum while achieving  $4 \times 10^{12}\text{ Jones}$  at  $\lambda = 1240\text{ nm}$ , doubling the specific detectivity of previously reported colloidal quantum-dot (CQD) devices (Figure 13.8).

Habisreutinger et al. demonstrated single-walled carbon nanotubes (SWCNTs) as an effective HTL for perovskite solar cells by reducing grain boundaries and pinholes within the perovskite, reaching photocurrents up to  $20.8\text{ mA/cm}^2$  [61]. This work was later expanded upon by Li et al. through the incorporation of a nanonet of carbon nanotubes within the perovskite film itself, providing fast charge extraction in addition to decreasing the overall film resistance and, in turn, increasing responsivity and EQE [62]. Alwadai et al. utilized vertically oriented Gd-doped ZnO nanorods (NRs) within an  $\text{MAPbI}_3$  film for a UV-to-IR photodetector (Figure 13.9) [63]. NRs simultaneously act as a UV absorptive material and

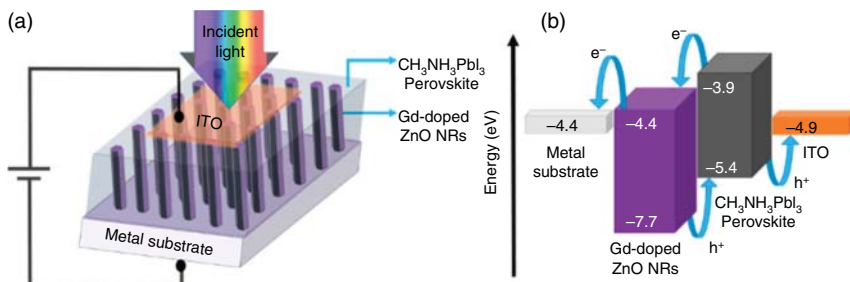


**Figure 13.9** (a) Schematic design of the photodetector architecture. (b) Energy level diagram of photodetector. Source: Alwadai et al. [63].

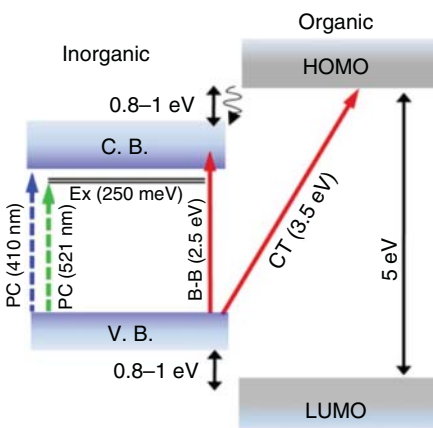


**Figure 13.10** Energy level diagram showing the broadband, charge transfer, and exciton bands of a 2D inorganic–organic perovskite. Source: Ahmad et al. [64]. Licensed under CC BY 4.0.

an ETL. The photodetector demonstrates a Fano-like intraband transition centered at  $\sim 1357$  nm for  $\text{MAPbI}_3$ . These photodetectors achieved responsivities and specific detectivities of  $28 \text{ A/W}$  and  $0.22 \text{ A/W}$  and  $1.2 \times 10^{12} \text{ Jones}$  and  $9.3 \times 10^9 \text{ Jones}$  upon white and IR ( $1200 \leq \lambda \leq 1600 \text{ nm}$ ) illuminations.

Kanaujia and coworkers designed an Al or Au/ $(\text{C}_6\text{H}_9\text{C}_2\text{H}_4\text{NH}_3)_2\text{PbI}_4$ /ITO perovskite photodetector that exhibited a broadband response at  $300 \leq \lambda \leq 475 \text{ nm}$  due to band-to-band and charge-transfer absorption transitions (Figure 13.10) [64]. Despite high binding energies, the detector also displayed a narrowband response centered at  $\lambda = 521 \text{ nm}$  due to bound exciton transitions. Upon the incorporation of a spiro-OMeTAD HTL and combined compact  $\text{TiO}_2$  and mesoporous  $\text{TiO}_2$  ETL, the photodetector displayed an EQE of 36% in the broadband region and 10% at the exciton wavelength. Lim et al. report various quasi-2D  $(\text{PEA})_2(\text{MA})_{n-1}\text{Pb}_n\text{I}_{3n+1}$  perovskite photodiodes with  $n = 1$  to  $\infty$  [65]. The detectors operated under 0 V bias and achieved low dark current of  $10^{-9} \text{ A}$  ( $n = 1$ ) to  $10^{-7} \text{ A}$  ( $n \geq 6$ ) that increases slightly with  $n$  at  $n \geq 6$ . Both  $n = 60$  and  $n = \infty$  displayed incredibly similar performance in terms of specific detectivity and responsivity, reaching values of  $2.01 \times 10^{12} \text{ Jones}$  and  $0.53 \text{ A/W}$  and  $2.2 \times 10^{12} \text{ Jones}$  and  $0.56 \text{ A/W}$ , respectively.

### 13.3.1.2 Narrowband Photodiodes

Both Fang et al. [14] and Lin et al. [66] demonstrated filterless narrowband perovskite photodetectors (Figure 13.11a). Through altering the halide composition, the primary absorption onset could be tuned, allowing for bandgaps of blue to red wavelengths. Due to the high absorption coefficient and large surface trap density, above-bandgap photogenerated charges are generated mostly near the surface where they become quenched and trapped and recombine. Below-bandgap charge carriers are generated much deeper in the crystal where they are more efficiently collected by the anode, contributing to the high, longer-wavelength EQE. With a large enough bias, collection efficiency of shorter-wavelength photogenerated charges increased dramatically more than the longer-wavelength charge carriers, eventually leading to a broadband response (Figure 13.12). The bandgap peaks ranged from  $\lambda \sim 410 \text{ nm}$  ( $\text{MAPbCl}_3$ ) to  $\lambda \sim 630 \text{ nm}$  ( $\text{MAPbBr}_{6/7}\text{I}_{1/7}$ ) with a full

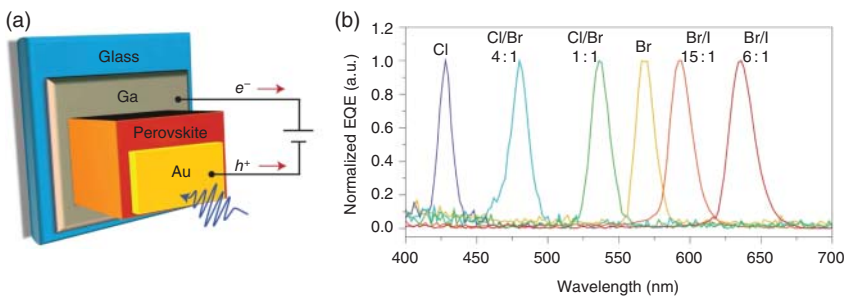


**Figure 13.11** (a) Schematic of device structure. (b) Normalized EQE spectra of single and mixed halide perovskite photodetectors with  $-1\text{ V}$  bias. Source: Fang et al. [14].

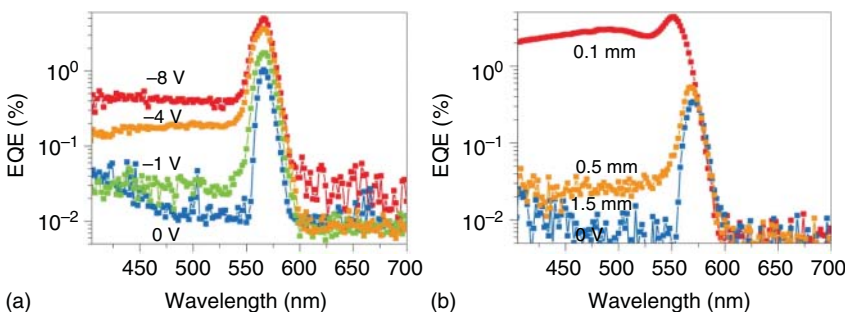


**Figure 13.12** (a) EQE spectra of 0.3 mm MAPbBr<sub>3</sub> single-crystal photodetector with  $-0.3\text{ V}$  bias. (b) EQE spectra of MAPbBr<sub>3</sub> single-crystal photodetectors with different thicknesses under  $-4\text{ V}$  bias. Source: Fang et al. [14].

width at half maximum (FWHM)  $<20\text{ nm}$  (Figure 13.11b) [14]. Halide composition tuning, however, does not tune the secondary absorption onset. Lin et al. added compatible organic small-molecule dyes, enabling tuning of both absorption edge onsets and full bandgap control. These narrowband photodetectors reached FWHM  $<100\text{ nm}$  in the response windows of  $400 \leq \lambda \leq 500\text{ nm}$ ,  $500 \leq \lambda \leq 600\text{ nm}$ , and  $600 \leq \lambda \leq 700\text{ nm}$  [66].

Li et al. demonstrated self-filtering narrowband photodetectors using an electronically inactive perovskite filter deposited on the substrate surface (Figure 13.13) [22]. The narrowband photodetector achieves a minimum FWHM of 28 nm that can be made larger. In addition, the detector maintains the superior specific detectivity, LDR, and response time of perovskite detectors of  $2.65 \times 10^{-12}\text{ Jones}$ , 190 dB, and 100 ns.

The photodetectors developed by Lin et al. displayed rather low maximum EQEs of  $\sim 12\%$  most likely due to the low charge carrier mobility of the organic molecules ( $\sim 6 \times 10^{-4}\text{ cm}^2/(\text{V s})$ ) [66]. In addition, the response time of the photodetectors developed by Fang et al. is limited by the crystal's thickness [14]. Qin et al. developed a double active layer photodetector utilizing both a polymer active layer and a perovskite electronically quenched, optically active layer (Figure 13.14) [67]. Within the perovskite, charge carriers are photogenerated and immediately quenched by

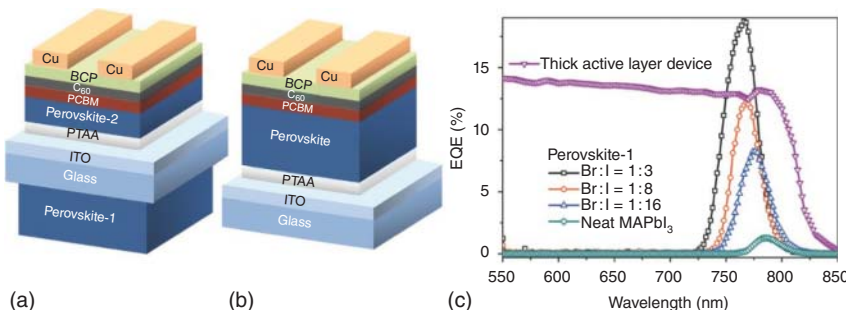


**Figure 13.13** (a) Device structure of self-filtered perovskite photodiode. (b) Device structure of wideband perovskite photodiode. (c) EQE demonstrates the conversion of wideband photodetector to narrowband photodetector using a perovskite filter. In addition, the fine-tuning of the EQE peak can be seen with change in halide composition. Source: Li et al. [22].

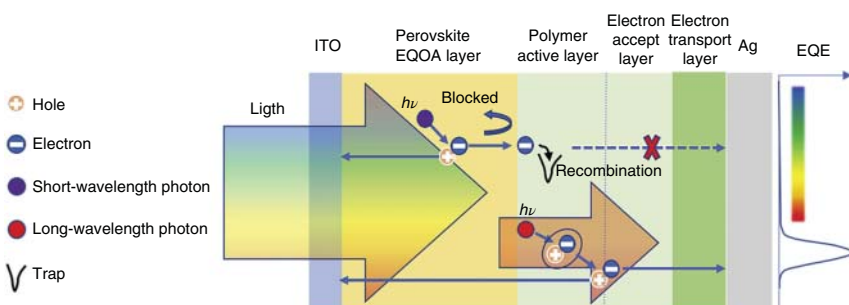


**Figure 13.14** Schematic of the working principle of the perovskite/polymer photodetector. Source: Qin et al. [67].

the thick and low-mobility polymer. As a result, only the absorption of polymer can induce a response in the photodetector. Therefore, the difference in polymer and perovskite absorption edges dictates the narrowband response range. The best detector demonstrated an EQE of  $\sim 20\%$  (Figure 13.15) with a FWHM of 70 nm in addition to a rise and fall time of 3.9 and 4.0  $\mu\text{s}$ , respectively.

### 13.3.2 Photoconductors

Photoconductors are a simple two-terminal p–n junction with either vertical or lateral device orientation. Vertical photoconductors (Figure 13.16a) have a small electrode spacing with a short carrier transit length, resulting in the fast response time and low driving voltage, while lateral photoconductors (Figure 13.16b–d) are the opposite but benefit from a larger photocurrent and are more easily manufactured [3].

Photoconductors are different from photodiodes in that they can exhibit a gain ( $G_{\text{ph}}$ ), which is particularly useful for applications with small signal such as single

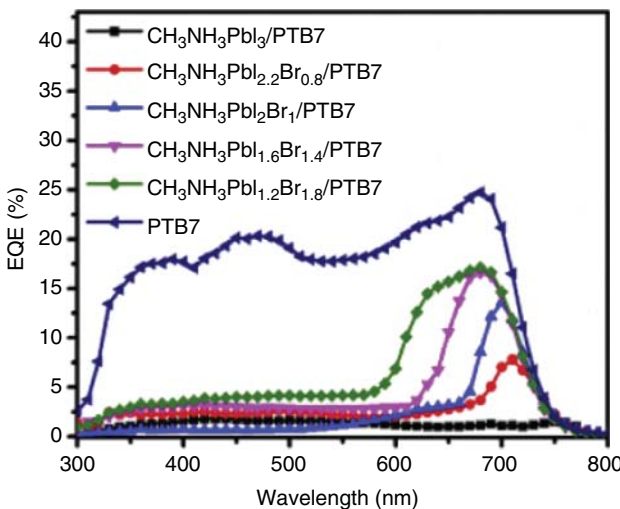


**Figure 13.15** EQE spectra of polymer/perovskite photodetectors with different halide concentrations. PTB7 is a benzodithiophene type semiconductive polymer. Source: Qin et al. [67].

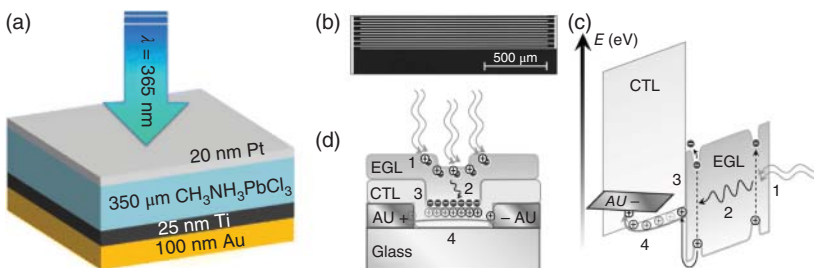


**Figure 13.16** (a) Vertical photoconductor device structure. Source: Maculan et al. [68]. (b) Lateral photoconductor device structure. Source: Ho et al. [69]. (c) Energy band diagram of a lateral bilayer heterojunction photoconductor operating at steady-state. Source: Ho et al. [69]. (d) A cross-sectional view of the same energy band diagram of a lateral bilayer heterojunction photoconductor operating at steady-state. Source: Ho et al. [69].

photon counting:

$$\Gamma_{\text{ph}} = \frac{I_{\text{ph}}}{qG_{\text{ph}}AL} = \frac{\tau_p}{t_n} \left( 1 + \frac{\mu_p}{\mu_n} \right) \quad (13.7)$$

where  $G_{\text{ph}}$  is the generation rate of excess carriers ( $\text{cm}^{-3} \text{s}^{-1}$ ),  $A$  is the cross-sectional area,  $L$  is the length,  $\tau_p$  is the excess minority carrier lifetime,  $t_n$  is the excess majority carrier transit time, and  $\mu_p$  and  $\mu_n$  are the minority and majority carrier mobilities, respectively. Gain enables an enhanced photocurrent and, in turn, large responsivity, though it does sacrifice the benefit of low dark current, resulting in the large NEP and small specific detectivity and LDR. Modern-day commercial photodetectors exhibiting high gain are generally expensive and laborious to produce, which could be dramatically improved via a solution-processed device.

### 13.3.2.1 Vertical Photoconductors

Moehl et al. were the first to show that photoconductive gain is possible using a vertical structure [70]. Devices were fabricated with either a porous or compact  $\text{TiO}_2$  HBL. The porous HBL allowed direct contact of  $\text{MAPbI}_3$  with the fluorine doped tin oxide (FTO) electrode and, in turn, charge injection into the perovskite under reverse bias. Charge injection resulted in a high dark current and photocurrent device, achieving a gain of  $\sim 150$  at low light intensities. A third device with no charge blocking layers expressed a photocurrent amplification of  $\sim 14$  fold, demonstrating that no charge blocking layer is possible for perovskite photoconductors.

Chen et al. developed a device that could switch between photovoltaic and photoconductive modes by changing the bias direction [71]. When operated at 0 V bias, the photodiode demonstrated high linearity. The detection range could be extended even more by operating in the photoconductive mode for low light intensities, demonstrating linearity up to  $0.1 \text{ mW/cm}^2$  with  $-0.7 \text{ V}$  bias and  $\lambda = 550 \text{ nm}$ . While in the reverse bias regime, the photocurrent displays a large linear dependence on bias magnitude. With a small incident power of  $2\text{--}20 \mu\text{W/cm}^2$ , the photodetector achieved an incredible gain of  $2400 \pm 100$ . The device exhibited a large, amplified photocurrent using bypass-rich  $\text{TiO}_2$  charge blocking layer while a high-density charge blocking layer suppressed current amplification. It was suggested that ferroelectric and piezoelectric dipole polarizations enabled the large photoconductive gain. Ishii et al. improved the performance by using a molecular layer of an Eu-terpy complex between the  $\text{MAPbI}_3$  nanocrystal absorber layer and the cathode [72]. This utilized trap-assisted charge tunneling injection at a heterogeneous interface to enable photomultiplication by contributing to a large leakage current (Figure 13.17). The photodetector achieved an EQE greater than  $2 \times 10^5\%$  at  $400 \leq \lambda \leq 750 \text{ nm}$  with  $-0.5 \text{ V}$  bias and a maximum of  $9 \times 10^5\%$  under an incident light intensity of  $0.76 \text{ mW/cm}^2$ , maintaining similar performance down to  $10 \mu\text{W/cm}^2$  incident light intensity.

Using a  $\text{TiO}_2$  MP scaffold HTL, Domanski et al. further optimized the design, obtaining a responsivity of  $208 \text{ A/W}$  at  $\lambda = 550 \text{ nm}$ , corresponding to an incident

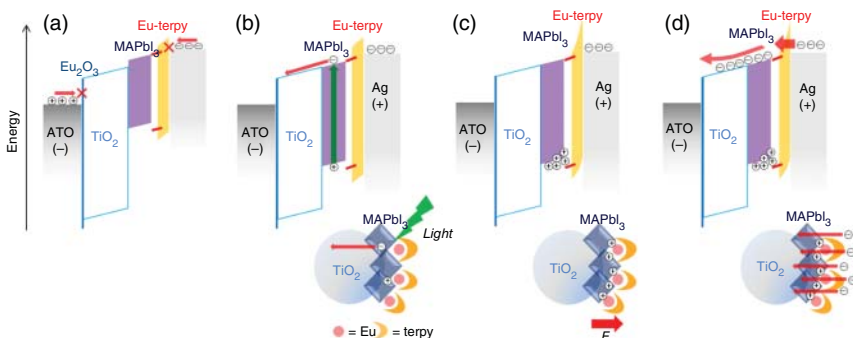


**Figure 13.17** Photomultiplication process of Eu-terpy complex photodetector under applied reverse bias. (a) Dark condition, (b) light absorption and carrier generation, (c) hole trapping and accumulation at the interface, and (d) charge tunneling injection from the cathode. Source: Ishii et al. [72].

photon-to-current efficiency (IPCE) of 47 000 [73]. The increased performance was explained to be from a charge buildup at the perovskite/FTO interface, increasing conductivity and lowering the FTO work function, which increased the hole current due to the direct hole injection.

Using a  $\text{MAPbI}_3$  perovskite, Dong et al. created a device with high responsivity without an interfacial electron-blocking layer (Figure 13.18a) [20]. Through utilizing density-functional theory calculations and by varying the  $\text{PbI}_2$  precursor concentration, it was determined that  $\text{Pb}^{2+}$  cations act as hole traps at the top surface, enabling electron injection and large gain (Figure 13.18d,e). The detector could switch between high-gain photodetector under reverse bias and efficient photovoltaic device with a forward bias (Figure 13.18b,c). The gain increased from 0.3 at 0 V to  $489 \pm 6$  at  $-1$  V with a high responsivity of  $242 \text{ A/W}$  and broad response range from UV to nIR. Yang et al. developed a metal–semiconductor–metal (MSM) photoconductor without any interfacial layers [74]. With a  $-1.5$  V bias, the photodetector achieved  $\text{EQE} > 10\,000\%$  at  $300 \text{ nm} \leq \lambda \leq 800 \text{ nm}$  with a maximum of  $60\,000\%$  at  $\lambda \sim 380 \text{ nm}$ .

### 13.3.2.2 Lateral Photoconductors

Hu et al. developed the first perovskite-based photodetector using a flexible polyethylene terephthalate (PET) substrate with  $\text{MAPbI}_3$  deposited between a pair of conductive ITO (indium tin oxide) contacts (Figure 13.19a) [75]. Having broadband sensitivity, the photodetector reached EQEs and responsivities of  $1.19 \times 10^3\%$  and  $3.49 \text{ A/W}$  at  $\lambda = 365 \text{ nm}$  and  $5.84\%$  and  $0.0367 \text{ A/W}$  at  $\lambda = 780 \text{ nm}$  with a  $-3$  V bias. It was proposed that upon illumination, the local electric field at the perovskite/ITO Schottky barriers efficiently separates the charge carriers in addition to reducing recombination rate (Figure 13.19b). The larger carrier density reduces the energy barrier height, allowing a greater ability of charge carrier tunneling and transport that significantly increases conductivity (Figure 13.19c,d).

Wang et al. developed a MSM UV photoconductor utilizing  $\text{MAPbCl}_3$  [76]. The detector achieved a responsivity of  $7.56 \text{ A/W}$  at  $\lambda = 360 \text{ nm}$  with a  $-4$  V bias. It had a fast response speed of  $<50 \text{ ms}$  while maintaining a low dark current. Zhou et al. similarly used a MSM structure with  $n = 1, 2$ , and  $3$   $(\text{CH}_3(\text{CH}_2)_3\text{NH}_3)_2(\text{CH}_3\text{NH}_3)_{n-1}\text{Pb}_n\text{I}_{3n+1}$ -layered perovskite [77]. The decreasing bandgap with increasing  $n$  results in the ability to detect different regions of light. The  $n = 3$  photodetector demonstrates the best performance with rise and fall times of  $10.0$  and  $7.5$  ms respectively, responsivity of  $12.78 \text{ mA/W}$  under  $-30$  V bias and  $3.0 \text{ mW/cm}^2$  incident light intensity, and  $I_{\text{light}}/I_{\text{dark}}$  of  $1 \times 10^3$  with  $-10$  V bias.

Ramasamy et al. designed an all-inorganic  $\text{CsPbI}_3$  nanocrystal (NC) photodetector [78]. The photodetectors exhibited an on/off ratio of  $\sim 10^5$  and rise and decay times of  $24$  and  $29$  ms, respectively.  $\text{CsPbX}_3$  NC photodetectors were improved upon by Dong et al. who demonstrated orientation-dependent performance and enhanced photodetecting capabilities with the Au plasmonic effect [79]. From x-ray diffraction (XRD) measurements, it is demonstrated that centrifugal casting results in higher-order and more dense films than drop-coated films, increasing photocurrent from  $0.67$  to  $2.77 \mu\text{A}$  due to the increased mobility. Owing to the localized surface

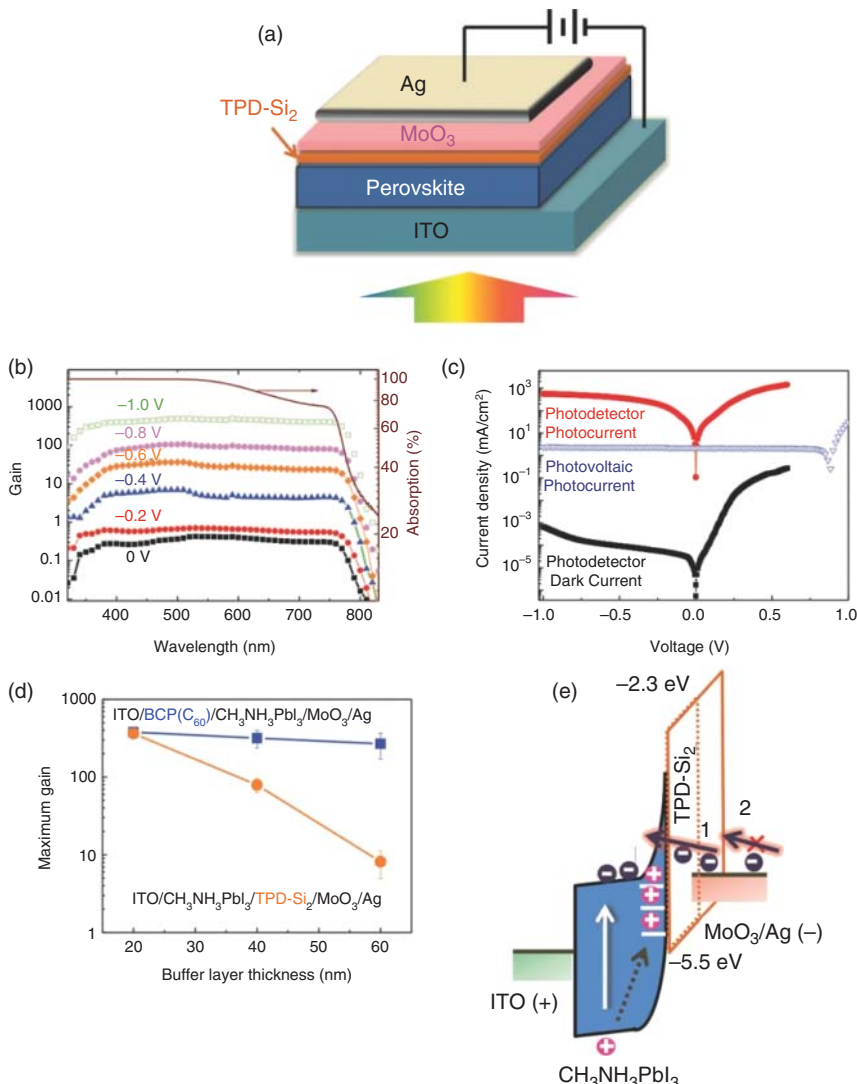


**Figure 13.18** (a) MAPbI<sub>3</sub> perovskite-based photoconductor structure. (b) Absorption spectrum of MAPbI<sub>3</sub> films and wavelength-dependent gain of the devices at different reverse biases between 0 and -1 V. (c) Photocurrent and dark current density for this photodetector and a reference photovoltaic device. (d) Dependence of gain on the thickness of the BCP passivating layer. (e) Band bending of the perovskite from charge accumulation under reverse bias and illumination. Source: Dong et al. [20].

plasmon resonance, Au-NC device exhibited an order of magnitude increased on/off ratio and an increase of photocurrent from 245.6 to 831.1 μA at -2 V bias with  $\lambda = 532$  nm.

Horváth et al. developed the first nanowire-based photodetector using slip-coated MAPbI<sub>3</sub> [80]. In the dark, the detector acted like a good insulator with currents on the order of tens of pA and resistances in the GΩ range. The responsivity and rise and

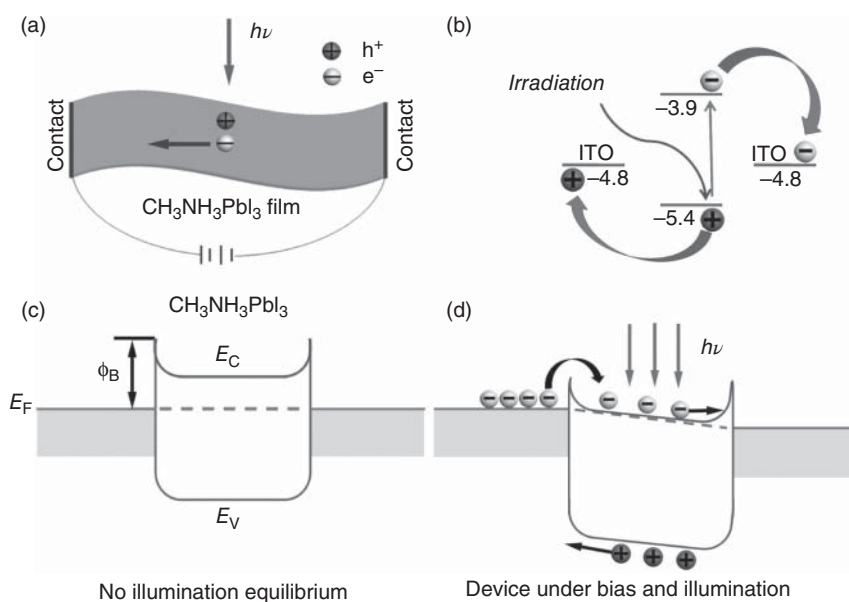


**Figure 13.19** (a) Schematic of  $\text{MAPbI}_3$  photoconductor. (b) Energy level diagram of photodetector. (c) Band diagram of Schottky barrier photoconductor at equilibrium. (d) Band diagram of Schottky barrier photoconductor under illumination. Source: Hu et al. [75].

fall times were 5 mA/W and under 500  $\mu\text{s}$ , respectively. Deng et al. utilized patterning via a mask and alignment of nanowires (NWs) by modified evaporation-induced self-assembly for the NW active layer [81]. Responsivity reached 0.85 A/W at  $-1$  V bias at a light intensity of  $4 \mu\text{W}/\text{cm}^2$ . Using a fluid-guided antisolvent vapor-assisted crystallization method, Deng et al. developed an  $\text{MAPb}(\text{I}_{1-x}\text{Br}_x)_3$  NW-array photoconductor whose NWs displayed smooth surfaces, a narrow width distribution, and a high degree of directional uniformity [82]. The photodetectors exhibited incredible performance of 12 500 A/W and LDR of 150 dB (Figure 13.20).

The lateral photoconductors discussed up to this point focus on detection of 300–900 nm light. Ka et al. utilized single-wall carbon nanotubes (SWCNTs)

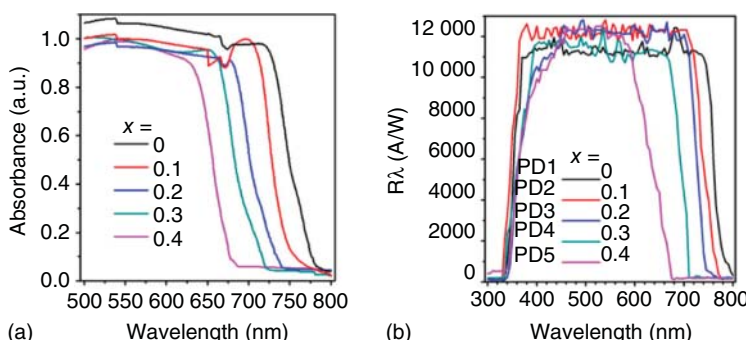


**Figure 13.20** (a) Absorption spectra of  $\text{MAPb}(\text{I}_{1-x}\text{Br}_x)_3$  NW arrays with  $0.0 \leq x \leq 0.4$ . (b) Responsivity of  $\text{MAPb}(\text{I}_{1-x}\text{Br}_x)_3$  NW array photodetectors. Source: Deng et al. [82].

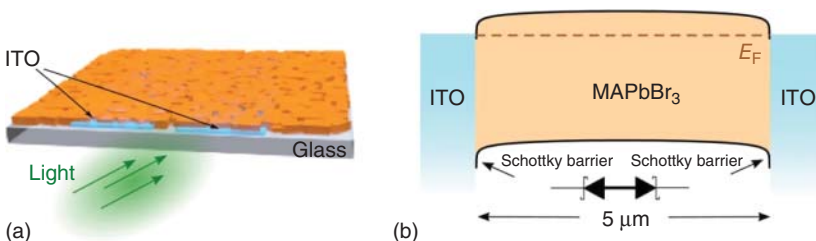


**Figure 13.21** (a) Structure of MAPbBr<sub>3</sub> single-crystal photodetector. (b) Energy level diagram demonstrating the formation of Schottky barriers between ITO interfaces to make a MSM structure. Source: Saidaminov et al. [89]. Licensed under CC BY 4.0.

decorated with PbS quantum dots embedded in an MAPbI<sub>3-x</sub>Cl<sub>x</sub> photoactive layer to extend the response range to  $\sim 1600$  nm and enable efficient charge transport [104]. A lower responsivity at higher incident light power is demonstrated, suggesting that the lower number of empty traps results in a reduction in the photoconductive gain. Pan et al. utilized erbium ytterbium silicate (EYS) nanosheets with MAPbI<sub>3</sub> perovskites to create a hybrid 2D-3D IR ( $1530 \leq \lambda \leq 1565$  nm) photodetector at the optical communication wavelength range [83]. In addition to converting IR light to visible light, EYS nanosheets act as a waveguide for the converted light, achieving a response time of  $900\text{ }\mu\text{s}$ .

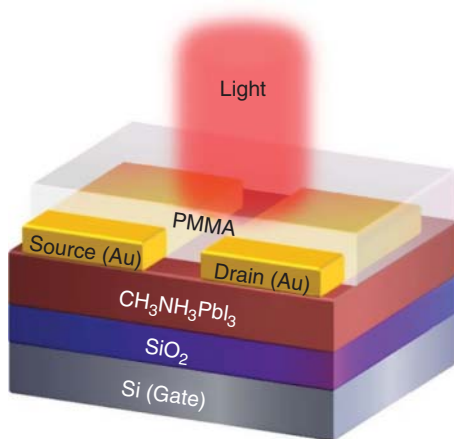
Qian et al. demonstrated the possibility of flexible, lead-free detectors with relatively good performance compared with the other similar flexible photoconductors [84]. These detectors employ 2D (PEA)<sub>2</sub>SnI<sub>4</sub> perovskites with 30 mol% SnF<sub>2</sub> added to reduce vacancies and improve stability. The devices achieved a responsivity of  $16\text{ A/W}$ , surpassing the previous maximum of  $3\text{ A/W}$  for flexible perovskite detectors with  $\lambda = 470$  nm [75, 85–87]. Lan et al. has published further work on 2D MAPbI<sub>3</sub> photodetectors that achieved a responsivity of  $40\text{ A/W}$  under  $405\text{ nm}$  incident light [88].

Due to the inherently large distance between electrodes for a lateral device, single crystals, with a typical thickness of millimeters, fill the role well for a superior active layer. Saidaminov et al. grew an MAPbBr<sub>3</sub> single crystal on top of an etched ITO-covered substrate using planar-integrated single-crystal growth method (Figure 13.21) [89]. The device displayed superior responsivity of  $4000\text{ A/W}$ . In addition, the detector achieved a relatively fast fall time of  $25\text{ }\mu\text{s}$  and a large specific detectivity of  $10^{13}\text{ Jones}$ . The detector's noise approaches the theoretical shot noise limit, showing that single crystals are potential low-noise solutions for inherently high-noise devices. Liu et al. demonstrated the use of 2D single-crystal (PEA)<sub>2</sub>PbI<sub>4</sub> for visible-light detection [90]. These single crystals showed anisotropic responsivities depending on the plane of fabrication with a maximum reaching as high as  $139.6\text{ A/W}$  on the (001) plane and a minimum dark current of  $3.06 \times 10^{-12}\text{ A}$ .

### 13.3.3 Phototransistor

Phototransistors have the same three-terminal structure as a field-effect transistor, consisting of a source, drain, and gate terminal (Figure 13.22), but with a photoactive

**Figure 13.22** Device structure of a bottom-gate, top-contact  $\text{MAPbI}_3$  perovskite phototransistor. Source: Li et al. [91]. Licensed under CC BY 4.0.



configuration. Under normal FET operation, the flow of accumulated current is controlled by the applied bias on the gate, enabling control over the flow of current due to the change in conductivity. A phototransistor can also control the charge carrier density and, in turn, conductivity through photoexcitation [92]. A phototransistor can exhibit high gain through the photogating effect where photogenerated charges are recirculated repeatedly before finally recombining [8, 93].

Though pure perovskite phototransistors have been developed, focus will be placed on the hybrid heterojunction structures due to their very noteworthy performance. The most notable of heterojunction phototransistors is the perovskite-graphene variety (Figure 13.23). Lee et al. fabricated a broadband UV-Vis phototransistor using a perovskite-graphene heterojunction [95]. The

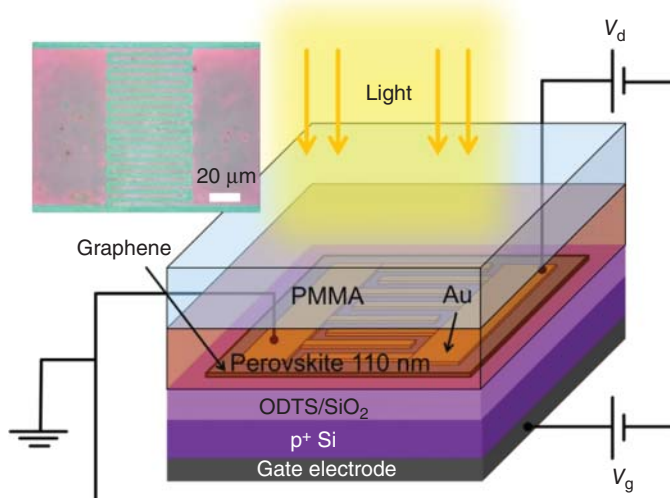


**Figure 13.23** Sample structure of a graphene–perovskite hybrid phototransistor. Source: Chang et al. [94]. Licensed under CC BY 4.0.

device achieved a high responsivity of  $180\text{ A/W}$ . It was discovered that graphene injects electrons to the perovskite valence band to fill the vacancies left behind by the photoexcited electrons now in the conduction band. These electrons are essentially trapped in the conduction band, producing photogating effects and gain. It has been demonstrated that integration of perovskite nanocrystals and nanowires into the graphene layer significant improves the performance [96–98].

Due to its high conductivity and lack of bandgap, graphene causes significant dark current in devices, so charge transport layers, namely, transition metal dichalcogenides (TMDs), can be used in place of graphene to reduce the noise. Using  $\text{WS}_2$ ,  $\text{WSe}_2$ , and  $\text{MoS}_2$ , photodetectors have achieved responsivities of 17, 950, and  $1.94 \times 10^6\text{ A/W}$  [99–102].  $\text{MoS}_2$  phototransistor achieved a large specific detectivity of  $1.29 \times 10^{12}\text{ Jones}$  at  $\lambda = 520\text{ nm}$  due to the significantly reduced dark current. Recently, Zhang et al. has integrated  $\text{WS}_2$  nanosheets into the perovskite layer for a perovskite–graphene heterojunction phototransistor [103]. Photoresponsivity increased to  $678.8\text{ A/W}$  while specific detectivity was  $4.99 \times 10^{11}\text{ Jones}$ . The authors attributed this high photoresponsivity to the electron–hole pair separation that is promoted by the selective electron trapping of  $\text{WS}_2$  nanosheets.

### 13.4 Conclusion

In addition to covering the basic elements of photodetectors and the theory behind their development, we have demonstrated how and why perovskites are a notable species for photodetector applications. We have touched on recent and notable progress made in the field of perovskite photodetectors. Even though these are a massive field of interest now, focus has mainly been placed on their photovoltaic applications in the past, leaving many large research opportunities in the photodetector field still available to pursue. With the seemingly ever growing and expanding field of perovskites, the interest in photodetectors to continually increase and rightfully so is expected. Perovskites are a highly competitive species in many optoelectronic applications and have continued to be proven so over the years.

### Acknowledgment

This material is based upon work supported by the Department of Energy/National Nuclear Security Administration under Award Number(s) DE-NA0003921.

### Disclaimer

“This report was prepared as an account of work sponsored by an agency of the US government. Neither the US government nor any agency thereof, nor any of their employees, makes any warranty, expressed or implied, assumes any legal liability or responsibility for the accuracy, completeness, or usefulness of any information,

apparatus, product, or process disclosed, or represents that its use would not infringe privately owned rights. Reference herein to any specific commercial product, process, or service by trade name, trademark, manufacturer, or otherwise does not necessarily constitute or imply its endorsement, recommendation, or favoring by the US government or any agency thereof. The views and opinions of authors expressed herein do not necessarily state or reflect those of the US government or any agency thereof.”

## References

- 1 (NREL) NREL. Best Research-Cell Efficiencies. <https://www.nrel.gov/pv/assets/pdfs/best-research-cell-efficiencies.20190802.pdf>.2020; <https://www.nrel.gov/pv/assets/pdfs/best-research-cell-efficiencies.20190802.pdf> (accessed 07 May 2021).
- 2 Poncea, C.S., Savenije, T.J., Abdellah, M. et al. (2014). Organometal halide perovskite solar cell materials rationalized: ultrafast charge generation, high and microsecond-long balanced mobilities, and slow recombination. *J. Am. Chem. Soc.* 136 (14): 5189–5192.
- 3 Wang, H. and Kim, D.H. (2017). Perovskite-based photodetectors: materials and devices. *Chem. Soc. Rev.* 46 (17): 5204–5236.
- 4 Brenner, T.M., Egger, D.A., Kronik, L. et al. (2016). Hybrid organic-inorganic perovskites: low-cost semiconductors with intriguing charge-transport properties. *Nat. Rev. Mater.* 1 (1): 1–16. <https://doi.org/10.1038/natrevmats.2015.7>.
- 5 Chen, B., Rudd, P.N., Yang, S. et al. (2019). Imperfections and their passivation in halide perovskite solar cells. *Chem. Soc. Rev.* 48 (14): 3842–3867.
- 6 Konstantatos, G. (2018). Current status and technological prospect of photodetectors based on two-dimensional materials. *Nat. Commun.* 9 (1): 9–11. <https://doi.org/10.1038/s41467-018-07643-7>.
- 7 Lei, B., Eze, V.O., and Mori, T. (2015). High performance  $\text{CH}_3\text{NH}_3\text{PbI}_3$  perovskite solar cells fabricated under ambient conditions with high relative humidity. *Jpn. J. Appl. Phys.* 54: 100305, 1–4.
- 8 Konstantatos, G. and Sargent, E.H. (2010). Nanostructured materials for photon detection. *Nat. Nanotechnol.* 5: 391–400.
- 9 Wolanyk, J., Xiao, X., Fralaide, M. et al. (2020). Tunable perovskite-based photodetectors in optical sensing. *Sens. Actuators, B* 321: 1–7.
- 10 Sarritzu, V., Sestu, N., Marongiu, D. et al. (2018). Direct or indirect bandgap in hybrid lead halide perovskites? *Adv. Opt. Mater.* 6: 1–8.
- 11 Leguy, A.M.A., Azarhoosh, P., Alonso, M.I. et al. (2016). Experimental and theoretical optical properties of methylammonium lead halide perovskites. *Nanoscale* 8 (12): 6317–6327.
- 12 Wang, T., Daiber, B., Frost, J.M. et al. (2017). Indirect to direct bandgap transition in methylammonium lead halide perovskite. *Energy Environ. Sci.* 10 (2): 509–515.

- 13 Motta, C., El-Mellouhi, F., Kais, S. et al. (2015). Revealing the role of organic cations in hybrid halide perovskite  $\text{CH}_3\text{NH}_3\text{PbI}_3$ . *Nat. Commun.* 6: 1–7. <https://doi.org/10.1038/ncomms8026>.
- 14 Fang, Y., Dong, Q., Shao, Y. et al. (2015). Highly narrowband perovskite single-crystal photodetectors enabled by surface-charge recombination. *Nat. Photonics* 9 (10): 679–686.
- 15 Zhang, M., Zhang, F., Wang, Y. et al. (2018). High-performance photodiode-type photodetectors based on polycrystalline formamidinium lead iodide perovskite thin films. *Sci. Rep.* 8 (1): 1–9.
- 16 Park, J.S. and Walsh, A. (2019). Embrace your defects. *Nat. Energy* 4 (2): 95–96. <https://doi.org/10.1038/s41560-019-0329-y>.
- 17 Kang, J. and Wang, L.W. (2017). High defect tolerance in lead halide perovskite  $\text{CsPbBr}_3$ . *J. Phys. Chem. Lett.* 8 (2): 489–493.
- 18 Oga, H., Saeki, A., Ogomi, Y. et al. (2014). Improved understanding of the electronic and energetic landscapes of perovskite solar cells: high local charge carrier mobility, reduced recombination, and extremely shallow traps. *J. Am. Chem. Soc.* 136 (39): 13818–13825.
- 19 Herz, L.M. (2017). Charge-carrier mobilities in metal halide perovskites: fundamental mechanisms and limits. *ACS Energy Lett.* 2 (7): 1539–1548.
- 20 Dong, R., Fang, Y., Chae, J. et al. (2015). High-gain and low-driving-voltage photodetectors based on organolead triiodide perovskites. *Adv. Mater.* 27 (11): 1912–1918.
- 21 Yadav, P., Prochowicz, D., Saliba, M. et al. (2017). Interfacial kinetics of efficient perovskite solar cells. *Crystals.* 7 (8): 252–260.
- 22 Li, L., Deng, Y., Bao, C. et al. (2017). Self-filtered narrowband perovskite photodetectors with ultrafast and tuned spectral response. *Adv. Opt. Mat.* 5: 1700672, 1–6.
- 23 Hwang, T., Yun, A.J., Kim, J. et al. (2019). Electronic traps and their correlations to perovskite solar cell performance via compositional and thermal annealing controls. *ACS Appl. Mater. Interfaces.* 11 (7): 6907–6917.
- 24 Armin, A., Juska, G., Philippa, B.W. et al. (2013). Doping-induced screening of the built-in-field in organic solar cells: effect on charge transport and recombination. *Adv. Energy Mater.* 3: 321–327.
- 25 Belisle, R.A., Nguyen, W.H., Bowring, A.R. et al. (2017). Interpretation of inverted photocurrent transients in organic lead halide perovskite solar cells: proof of the field screening by mobile ions and determination of the space charge layer widths. *Energy Environ. Sci.* 10: 192–204.
- 26 Eames, C., Frost, J.M., Barnes, P.R.F. et al. (2015). Ionic transport in hybrid lead iodide perovskite solar cells. *Nat. Commun.* 6: 1–8.
- 27 Calado, P., Telford, A.M., Bryant, D. et al. (2016). Evidence for ion migration in hybrid perovskite solar cells with minimal hysteresis. *Nat. Commun.* 7: 1–10.
- 28 Von Hauff, E. (2019). Impedance spectroscopy for emerging photovoltaics. *J. Phys. Chem. C.* 123 (10): 11329–11346.
- 29 Yu, H., Lu, H., Xie, F. et al. (2016). Native defect-induced hysteresis behavior in organolead iodide perovskite solar cells. *Adv. Funct. Mater.* 26: 1411–1419.

- 30** Gottesman, R., Lopez-Varo, P., Gouda, L. et al. (2016). Dynamic phenomena at perovskite/electron-selective contact interface as interpreted from photovoltage decays. *Chem.* 1: 776–789.
- 31** Domanski, K., Roose, B., Matsui, T. et al. (2017). Migration of cations induces reversible performance losses over day/night cycling in perovskite solar cells. *Energy Environ. Sci.* 10: 604–613.
- 32** Almora, O., Aranda, C., Mas-Marzá, E. et al. (2016). On Mott-Schottky analysis interpretation of capacitance measurements in organometal perovskite solar cells. *Appl. Phys. Lett.* 109 (17): 1–5. <https://doi.org/10.1063/1.4966127>.
- 33** Yang, S., Chen, S., Mosconi, E. et al. (2019). Stabilizing halide perovskite surfaces for solar cell operation with wide-bandgap lead oxysalts. *Science* 365 (6452): 473–478.
- 34** Landi, G., Neitzert, H.C., Barone, C. et al. (2017). Correlation between electronic defect states distribution and device performance of perovskite solar cells. *Adv. Sci.* 4: 1700183, 1–11.
- 35** Hwang, T., Yun, A.J., Kim, J. et al. (2019). Electronic traps and their correlations to perovskite solar cell performance via compositional and thermal annealing controls. *ACS Appl. Mater. Interfaces* 11 (7): 6907–6917.
- 36** Shen, Q., Ng, A., Ren, Z. et al. (2018). Characterization of low-frequency excess noise in  $\text{CH}_3\text{NH}_3\text{PbI}_3$ -based solar cells grown by solution and hybrid chemical vapor deposition techniques. *ACS Appl. Mater. Interfaces* 10 (1): 371–380.
- 37** Sangwan, V.K., Zhu, M., Clark, S. et al. (2019). Low-frequency carrier kinetics in perovskite solar cells. *ACS Appl. Mater. Interfaces* 11 (15): 14166–14174.
- 38** Barone, C., Lang, F., Mauro, C. et al. (2016). Unravelling the low-temperature metastable state in perovskite solar cells by noise spectroscopy. *Sci. Rep.* 6: 1–8.
- 39** Yang, D. and Ma, D. (2019). Development of organic semiconductor photodetectors: from mechanism to applications. *Adv. Opt. Mater.* 7: 1–23.
- 40** Wakatsuki, A., Furuta, T., and Muramoto, Y. et al. (2009). High-speed photodiode and optical receiver technologies. *Conference on Optical Fiber Communication, Technical Digest Series*. 1–3.
- 41** Ji, F., Juntunen, M., and Hietanen, I. et al. (2007). Advanced photodiode detector for medical CT imaging: design and performance. *IEEE International Symposium on Industrial Electronics*. 2730–2735.
- 42** Hoang, A.M., Dehzangi, A., Adhikary, S. et al. (2016). High performance bias-selectable three-color Short-wave/Mid-wave/Long-wave infrared Photodetectors based on Type-II InAs/GaSb/AlSb superlattices. *Sci. Rep.* 6: 1–7.
- 43** Sun, Q., Dong, G., Li, D. et al. (2012). Dark current and photovoltage models on the formation of depletion region in  $\text{C}_{60}/\text{NPB}$  organic heterojunctions. *Org. Electron.* 13 (12): 3276–3283. <https://doi.org/10.1016/j.orgel.2012.09.022>.
- 44** Yuan, D.X., Yuan, X.D., Xu, Q.Y. et al. (2015). A solution-processed bathocuproine cathode interfacial layer for high-performance bromine-iodine perovskite solar cells. *Phys. Chem. Chem. Phys.* 17 (40): 26653–26658.
- 45** Bao, C., Chen, Z., Fang, Y. et al. (2017). Low-noise and large-linear-dynamic-range photodetectors based on hybrid-perovskite thin-single-crystals. *Adv. Mater.* 29: 1–7.

- 46** Fang, Y. and Huang, J. (2015). Resolving weak light of sub-picowatt per square centimeter by hybrid perovskite photodetectors enabled by noise reduction. *Adv. Mater.* 27 (17): 2804–2810.
- 47** Dou, L., Yang, Y.M., You, J. et al. (2014). Solution-processed hybrid perovskite photodetectors with high detectivity. *Nat. Commun.* 5: 1–6.
- 48** Gong, X. (2015). Ultrasensitive solution-processed perovskite hybrid photodetectors. *J. Mater. Chem. C* 3 (26): 6600–6606.
- 49** Teng, F., Chen, Q., Chen, L. et al. (2016). Mixture interlayer for high performance organic-inorganic perovskite photodetectors. *Applied Physics Letters* 109: 123301, 1–4. <https://doi.org/10.1063/1.4963269>.
- 50** Wang, Q., Shao, Y., Dong, Q. et al. (2014). Large fill-factor bilayer iodine perovskite solar cells fabricated by a low-temperature solution-process. *Energy Environ. Sci.* 7: 2359–2365.
- 51** Lin, Q., Armin, A., Lyons, D.M. et al. (2015). Low noise, IR-blind organohalide perovskite photodiodes for visible light detection and imaging. *Adv. Mater.* 27: 2060–2064.
- 52** Chen, Z., Dong, Q., Liu, Y. et al. (2017). Thin single crystal perovskite solar cells to harvest below-bandgap light absorption. *Nat. Commun.* 8: 1–7.
- 53** Shen, L., Lin, Y., Bao, C. et al. (2017). Integration of perovskite and polymer photoactive layers to produce ultrafast response, ultraviolet-to-near-infrared, sensitive photodetectors. *Mater. Horiz.* 4: 242–248.
- 54** Su, L., Zhao, Z.X., Li, H.Y. et al. (2015). High-performance organolead halide perovskite-based self-powered triboelectric photodetector. *ACS Nano* 9 (11): 11310–11316.
- 55** Gao, P., Grätzel, M., and Nazeeruddin, M.K. (2014). Organohalide lead perovskites for photovoltaic applications. *Energy Environ. Sci.* 7: 2448–2463.
- 56** Zhang, J.Y., Xu, J.L., Chen, T. et al. (2019). Toward broadband imaging: surface-engineered PbS quantum dot/perovskite composite integrated ultrasensitive photodetectors. *ACS Appl. Mater. Interfaces* 11 (47): 44430–44437.
- 57** Liu, C., Wang, K., Du, P. et al. (2015). Ultrasensitive solution-processed broad-band photodetectors using  $\text{CH}_3\text{NH}_3\text{PbI}_3$  perovskite hybrids and PbS quantum dots as light harvesters. *Nanoscale* 7: 16460–16469.
- 58** Ning, Z., Gong, X., Comin, R. et al. (2015). Quantum-dot-in-perovskite solids. *Nature* 523: 324–328.
- 59** Clifford, J.P., Konstantatos, G., Johnston, K.W. et al. (2008). Fast, sensitive and spectrally tuneable colloidal-quantum-dot photodetectors. *Nat. Nanotechnol.* 4: 3–7.
- 60** Pelayo, F., de Arquer, G., Gong, X. et al. (2017). Field-emission from quantum-dot-in-perovskite solids. *Nat. Commun.* 8: 1–8.
- 61** Habisreutinger, S.N., Leijtens, T., Eperon, G.E. et al. (2014). Carbon nanotube/polymer composites as a highly stable hole collection layer in perovskite solar cells. *Nano Lett.* 14: 5561–5568.
- 62** Li, X., Yu, D., Chen, J. et al. (2017). Constructing fast carrier tracks into flexible perovskite photodetectors to greatly improve responsivity. *ACS Nano* 11: 2015–2023.

- 63** Alwadai, N., Haque, M.A., Mitra, S. et al. (2017). High-performance ultraviolet-to-infrared broadband perovskite photodetectors achieved via inter-/intraband transitions. *ACS Appl. Mater. Interfaces* 9: 37832–37838.
- 64** Ahmad, S., Kanaujia, P.K., Beeson, H.J. et al. (2015). Strong photocurrent from two-dimensional excitons in solution- processed stacked perovskite semiconductor sheets. *ACS Appl. Mater. Interfaces* 7: 25227–25236.
- 65** Lim, J.W., Wang, H., Choi, C.H. et al. (2019, 2018). Self-powered reduced-dimensionality perovskite photodiodes with controlled crystalline phase and improved stability. *Nano Energy* 57: 761–770. <https://doi.org/10.1016/j.nanoen.2018.12.068>.
- 66** Lin, Q., Armin, A., Burn, P.L. et al. (2015). Filterless narrowband visible photodetectors. *Nat. Photonics.* 9: 687–694.
- 67** Qin, Z., Song, D., Xu, Z. et al. (2020, 2019). Filterless narrowband photodetectors employing perovskite / polymer synergetic layers with tunable spectral response. *Org. Electron.* 76: 105417. <https://doi.org/10.1016/j.orgel.2019.105417>.
- 68** Maculan, G., Sheikh, A.D., Abdelhady, A.L. et al. (2015).  $\text{CH}_3\text{NH}_3\text{PbCl}_3$  single crystals: inverse temperature crystallization and visible-blind UV-photodetector. *J. Phys. Chem. Lett.* 6 (19): 3781–3786.
- 69** Ho, J.C., Arango, A., and Bulović, V. (2008). Lateral organic bilayer heterojunction photoconductors. *Appl. Phys. Lett.* 93 (6): 063305, 1–3.
- 70** Moehl, T., Im, J.H., Lee, Y.H. et al. (2014). Strong photocurrent amplification in perovskite solar cells with a porous  $\text{TiO}_2$  blocking layer under reverse bias. *J. Phys. Chem. Lett.* 5 (21): 3931–3936.
- 71** Chen, H.W., Sakai, N., Jena, A.K. et al. (2015). A switchable high-sensitivity photodetecting and photovoltaic device with perovskite absorber. *J. Phys. Chem. Lett.* 6 (9): 1773–1779.
- 72** Ishii, A., Jena, A.K., and Miyasaka, T. (2019). Photomultiplying visible light detection by halide perovskite nanoparticles hybridized with an organo Eu complex. *J. Phys. Chem. Lett.* 10: 5935–5942.
- 73** Domanski, K., Tress, W., Moehl, T. et al. (2015). Working principles of perovskite photodetectors: analyzing the interplay between photoconductivity and voltage- driven energy-level alignment. *Adv. Funct. Mater.* 25: 6936–6947.
- 74** Yang, J., Yu, T., Zhu, K. et al. (2017). High-gain and fast-response metal-semiconductor-metal structured organolead halide perovskite photodetectors. *J. Phys. D: Appl. Phys.* 50: 1–7.
- 75** Hu, X., Zhang, X., Liang, L. et al. (2014). High-performance flexible broadband photodetector based on organolead halide perovskite. *Adv. Funct. Mater.* 24: 7373–7380.
- 76** Wang, W., Xu, H., Cai, J. et al. (2016). Visible blind ultraviolet photodetector based on  $\text{CH}_3\text{NH}_3\text{PbCl}_3$  thin film. *Opt. Express* 24 (8): 8411.
- 77** Zhou, J., Chu, Y., and Huang, J. (2016). Photodetectors based on two-dimensional layer-structured hybrid lead iodide perovskite semiconductors. *ACS Appl. Mater. Interfaces* 8 (39): 25660–25666.

- 78** Ramasamy, P., Lim, D.H., Kim, B. et al. (2016). All-inorganic cesium lead halide perovskite nanocrystals for photodetector applications. *Chem. Commun.* 52 (10): 2067–2070.
- 79** Dong, Y., Gu, Y., Zou, Y. et al. (2016). Improving all-inorganic perovskite photodetectors by preferred orientation and plasmonic effect. *Small* 12 (40): 5622–5632.
- 80** Horváth, E., Spina, M., Szekrényes, Z. et al. (2014). Nanowires of methylammonium lead iodide ( $\text{CH}_3\text{NH}_3\text{PbI}_3$ ) prepared by low temperature solution-mediated crystallization. *Nano Lett.* 14 (12): 6761–6766.
- 81** Deng, H., Dong, D., Qiao, K. et al. (2015). Growth, patterning and alignment of organolead iodide perovskite nanowires for optoelectronic devices. *Nanoscale* 7 (9): 4163–4170.
- 82** Deng, W., Huang, L., Xu, X. et al. (2017). Ultrahigh-responsivity photodetectors from perovskite nanowire arrays for sequentially tunable spectral measurement. *Nano Lett.* 17 (4): 2482–2489.
- 83** Zhang, X., Yang, S., Zhou, H. et al. (2017). Perovskite–erbium silicate nanosheet hybrid waveguide photodetectors at the near-infrared telecommunication band. *Adv. Mater.* 29 (21): 1–8.
- 84** Qian, L., Sun, Y., Wu, M. et al. (2018). A lead-free two-dimensional perovskite for a high-performance flexible photoconductor and a light-stimulated synaptic device. *Nanoscale* 10: 6837–6843. <https://doi.org/10.1039/c8nr00914g>.
- 85** Sun, H., Lei, T., Tian, W. et al. (2017). Perovskite photodetector based on low-cost carbon cloth. *Small* 13: 1701042, 1–7.
- 86** Cheng, Y., Tang, J., and Song, H. (2015). Flexible and semitransparent organolead triiodide perovskite network photodetector arrays with high stability. *Nano Lett.* 15 (12): 7963–7969.
- 87** Chen, S., Teng, C., Zhang, M. et al. (2016). A flexible UV–Vis–NIR photodetector based on a perovskite / conjugated-polymer composite. *Composite. Adv. Mater.* 28: 5969–5974.
- 88** Lan, C., Dong, R., Zhou, Z. et al. (2017). Large-scale synthesis of freestanding layer-structured  $\text{PbI}_2$  and  $\text{MAPbI}_3$  nanosheets for high-performance photodetection. *Adv. Mater.* 29: 1702759, 1–9.
- 89** Saidaminov, M.I., Adinolfi, V., Comin, R. et al. (2015). Planar-integrated single-crystalline perovskite photodetectors. *Nat. Commun.* 6: 4–10.
- 90** Liu, Y., Ye, H., Zhang, Y. et al. (2019). Surface-tension-controlled crystallization for high-quality 2D perovskite single crystals for ultrahigh photodetection surface-tension-controlled crystallization for high-quality 2D perovskite single crystals for ultrahigh photodetection. *Matter* 1 (2): 465–480. <https://doi.org/10.1016/j.matt.2019.04.002>.
- 91** Li, F., Ma, C., Wang, H. et al. (2015). Ambipolar solution-processed hybrid perovskite phototransistors. *Nat. Commun.* 6: 1–8.
- 92** Xie, C., You, P., Liu, Z. et al. (2017). Ultrasensitive broadband phototransistors based on perovskite/organic-semiconductor vertical heterojunctions. *Light Sci. Appl.* 6 (8): e17023, 1–9.

- 93** Soci, C., Zhang, A., Xiang, B. et al. (2007). ZnO nanowire UV photodetectors with high internal gain. *Nano Lett.* 7: 1003–1009.
- 94** Chang, P.H., Liu, S.Y., Lan, Y.B. et al. (2017). Ultrahigh responsivity and detectivity graphene-perovskite hybrid phototransistors by sequential vapor deposition. *Sci. Rep.* 7: 1–10.
- 95** Lee, Y., Kwon, J., Hwang, E. et al. (2015). High-performance perovskite-graphene hybrid photodetector. *Adv. Mater.* 27: 41–46.
- 96** Sun, Z., Aigouy, L., and Chen, Z. (2016). Plasmonic-enhanced perovskite-graphene hybrid photodetectors. *Nanoscale*. 8: 7377–7383.
- 97** Kwak, D.H., Lim, D.H., Ra, H.S. et al. (2016). High performance hybrid graphene- $\text{CsPbBr}_{3-x}\text{I}_x$  perovskite nanocrystal photodetector. *RSC Adv.* 6: 65252–65256.
- 98** Spina, M., Lehmann, M., Náfrádi, B. et al. (2015). Microengineered  $\text{CH}_3\text{NH}_3\text{PbI}_3$  nanowire/graphene phototransistor for low-intensity light detection at room temperature. *Small*. 11 (37): 4824–4828.
- 99** Ma, C., Shi, Y., Hu, W. et al. (2016). Heterostructured  $\text{WS}_2/\text{CH}_3\text{NH}_3\text{PbI}_3$  photoconductors with suppressed dark current and enhanced photodetectivity. *Adv. Mater.* 28: 3683–3689.
- 100** Cheng, H.C., Wang, G., Li, D. et al. (2016). Van der Waals heterojunction devices based on organohalide perovskites and two-dimensional materials. *Nano Lett.* 16 (1): 367–373.
- 101** Kang, D.H., Pae, S.R., Shim, J. et al. (2016). An ultrahigh-performance photodetector based on a perovskite–transition-metal-dichalcogenide hybrid structure. *Adv. Mater.* 28: 7799–7806.
- 102** Liu, F., Wang, J., Wang, L. et al. (2017). Enhancement of photodetection based on perovskite/ $\text{MoS}_2$  hybrid thin film transistor. *J. Semicond.* 38 (3): 1–6.
- 103** Zhang, D. and Yu, R. (2019). Perovskite- $\text{WS}_2$  nanosheet composite optical absorbers on graphene as high-performance phototransistors. *Front. Chem.* 7: 1–6.
- 104** Ka, I., Gerlein, L., Asuo, I. et al. (2018). An ultra-broadband perovskite-PbS quantum dot sensitized carbon nanotube photodetector. *Nanoscale* 10: 9044–9052.